Journal of Microscopy, Vol. 233, Pt 2 2009, pp. 331–339
Received 2 June 2008; accepted 7 October 2008

Analysis of 3D elemental mapping artefacts in biological specimens using Monte Carlo simulation

K. SCOTT & N.W.M. RITCHIE
National Institute of Standards and Technology, 100 Bureau Drive, Gaithersburg, MD 20899, U.S.A.

Key words. Diatom, EDS, FIB, focused ion beam, Monte Carlo, SEM, X-ray microanalysis, 3D elemental mapping.

Summary

In this paper, we present Monte Carlo simulation results demonstrating the feasibility of using the focused ion beam based X-ray microanalysis technique (FIB-EDS) for the 3D elemental analysis of biological samples. In this study, we used a marine diatom *Thalassiosira pseudonana* as our model organism and NISTMonte for the Monte Carlo simulations. We explored several beam energies commonly used for the X-ray microanalysis to examine their effects on the resulting 3D elemental volume of the model organism. We also performed a preliminary study on the sensitivity of X-ray analysis for detecting nanoparticles in the model. For the conditions considered in this work, we show that the X-ray mapping performed using the 5 keV beam energy results in 3D elemental distributions that closely reflect the elemental distributions in the original model. At 5 keV, the depth resolution of the X-ray maps is about 250 nm for the model organism. We also show that the nanoparticles that are 50 nm in diameter or greater are easily located. Although much work is still needed in generating more accurate biological models and simulating experimental conditions relevant to these samples, our results indicate that FIB-EDS is a promising technique for the 3D elemental analysis of some biological specimens.

Introduction

Accurate 3D characterization of cellular structure and chemistry is essential for understanding cellular behaviour and processes. The complexity of and variability among cellular structures and the presence of microenvironments within the cellular matrices require 3D characterization data for the quantitative structural analysis of cells. For example, 3D imaging played an important role in the quantitative analysis of mitochondrial morphology and their contribution to tumorigenesis (Alirol & Martinou, 2006). The 3D structural analysis of Golgi organization helped to elucidate the role of this organelle in protein and lipid sorting and trafficking (Marsh *et al.*, 2001). A 3D biological characterization technique that can visualize details of the membrane structures, various organelles and their intra- and inter-cellular interactions can greatly enhance study of cellular physiology and processes. However, such a technique would require nanometre resolution and several tens of micrometre field of view.

Currently, transmission electron microscopy tomography and laser scanning confocal microscopy are the popular high-resolution 3D imaging techniques used for micro-structural analysis of biological specimens (Frank, 1992; McEwen & Marko, 2001; Baumeister, 2002; Leapman, 2004; Hell, 2003; Gustafsson, 2005; McIntosh *et al.*, 2005; Rust *et al.*, 2006; Shroff *et al.*, 2007). Ensemble techniques such as single particle electron cryo-microscopy (cryo-EM) and diffraction techniques like synchrotron based X-ray scattering are also commonly used to determine the 3D structural details of macromolecules such as proteins at near-atomic resolution (Svergun & Koch, 2002; Jiang *et al.*, 2008). Although transmission electron microscopy and ensemble techniques are well suited for high-resolution imaging of sub-cellular features and structural analysis of molecular complexes and laser scanning confocal microscopy is a good technique for cell population or tissue level analysis, none of these techniques can effectively perform *in situ* high-resolution imaging of features that are tens of micrometres in size, roughly the size of a mammalian cell. Focused ion beam scanning electron microscopy (FIB-SEM) provides a good bridging technique for this apparent resolution gap between the 100-nm-resolution laser scanning confocal microscopy and the sub-nanometre resolution transmission electron microscopy techniques (Subramaniam, 2005).

FIB-SEM is a technique where the imaging capability of SEM is combined with the cutting and deposition capability of an FIB. In an FIB-SEM instrument, a precise amount of the sample material at a specific location can be removed or milled away

Correspondence to: Keana Scott. Tel: 301 975 4579; fax: 301 926 6689; e-mail: keana.scott@nist.gov

to create a new surface using a focused ion beam. This newly created surface can then be imaged using either the ion beam or the electron beam. Three-dimensional images of a sample can be obtained by repeating this process of milling a thin layer of the sample material using the FIB and then imaging the newly exposed surface with an SEM. The sample volume that can be imaged using this technique is limited mainly by the milling rate and the desired lateral resolution. Depending on the material, FIB-SEM can reliably perform at 15 nm milling (depth) resolution and 10 to 20 nm lateral resolution (Uchic *et al.*, 2007).

For many years, site specific milling and imaging using FIB-SEM has been employed by materials scientists and the semiconductor industry to great advantage (Volkert & Minor, 2007). More recently, high precision sequential milling and imaging have been effectively used to study the 3D microstructure of metals, ceramics and other inorganic materials (Holzer *et al.*, 2004). FIB-SEM instruments can also be equipped with an energy dispersive X-ray spectrometer (EDS) and provide not only the 3D structural details of the sample but also the 3D elemental distributions in the sample. Recent studies have successfully demonstrated this 3D FIB-EDS technique on a Cu–Ag eutectic alloy sample by sequentially milling away layers of material, imaging the newly exposed surfaces and collecting spectrum images of the surfaces (Kotula *et al.*, 2006).

Recently, 3D reconstruction of a budding yeast cell was successfully demonstrated using FIB-SEM (Heymann *et al.*, 2006). In another study, the 3D structure of bone/dental implant interfaces was analysed using the FIB-SEM technique (Giannuzzi *et al.*, 2007). However, the high-resolution 3D imaging of cellular morphology using FIB-SEM is a relatively new development and the use of the FIB-EDS technique for the analysis of 3D elemental distributions (X-ray microanalysis) has not been applied to bulk biological specimens.

In this paper, we present Monte Carlo simulation results of the FIB-EDS based 3D X-ray microanalysis of biological samples. We explored various beam energies commonly used for X-ray microanalysis to examine their effects on the resulting 3D elemental volume of a model organism. We also performed a preliminary study on the sensitivity of X-ray analysis for detecting nanoparticles in the model.

Materials and methods

Use of Monte Carlo simulations for X-ray microanalysis

X-ray microanalysis of thin-sectioned or cryo-fractured biological specimens is a well established technique. The ability to spatially resolve and quantify the diffusible and physiologically active elements within the sample has been useful for studying the role of chemical signalling in cellular processes (LeFurgey *et al.*, 1988; Zierold *et al.*, 2005). However, X-ray microanalysis of biological specimens can be challenging because the physiologically active elements usually have low atomic numbers, are present in low concentrations and are easily removed during the sample preparation steps (Echlin, 1992). Also, the mapping artefacts due to the beam–sample interaction, the fractured sample surface topography and the complex sample morphology further complicate the proper interpretation of the experimental data. For example, if the electron beam energy is too high, e.g. 20 keV, the electrons would penetrate deep into the sample volume and excite X-rays from a region of the sample that is much larger than the region observed in the electron image, resulting in the degraded resolution of the X-ray elemental maps. It is crucial to understand and consider the possible artefacts, their magnitudes and their effects to perform an accurate 3D elemental analysis of bulk biological samples using X-ray microanalysis.

The behaviour of electrons hitting the sample surface and the generation of X-rays in the sample volume are well understood and many tools exist for modelling these phenomena for various experimental conditions (Goldstein *et al.*, 2003). For example, for a homogeneous flat bulk sample, the electron range in the sample can be estimated by a simple equation that is a function of the atomic number, the density, the beam energy and the tilt angle. Another widely used technique for estimating the beam–sample interaction volume and studying the electron trajectory in the sample volume is the Monte Carlo simulation of electron transport. There are several well known and useful implementations of Monte Carlo simulation for X-ray microanalysis (Myklebust *et al.*, 1976; Joy, 1995; Hovington *et al.*, 1997; Gauvin *et al.*, 2006; Ritchie, 2005a; Salvat *et al.*, 2006). For this study, we used a publicly available Monte Carlo simulation tool, NISTMonte, to model the electron beam induced X-ray generation in biological sample volumes (Ritchie, 2005a; 2008).

The spectrum simulation algorithm within NISTMonte depends upon models of electron transport, ionization, relaxation, X-ray transport and detection. Each of these models has been validated independently through comparison with published tables, charts and measured spectra as available and as appropriate (Ritchie, 2005b). The overall performance of the NISTMonte spectrum simulation has been validated by comparison with measured bulk spectra. The comparisons have demonstrated NISTMonte's ability to accurately simulate the relative intensity of characteristic lines to within about 20% in most cases and to within 50% in almost all cases. Exceptions include very low energy lines for which detector efficiency and absorption coefficients are poorly known.

Monte Carlo models

The model organism used for the Monte Carlo simulation is a eukaryotic unicellular marine diatom *Thalassiosira pseudonana*. These diatoms are cylinder shaped and about 4 μm in diameter and 7 μm in length. Their main feature is the finely

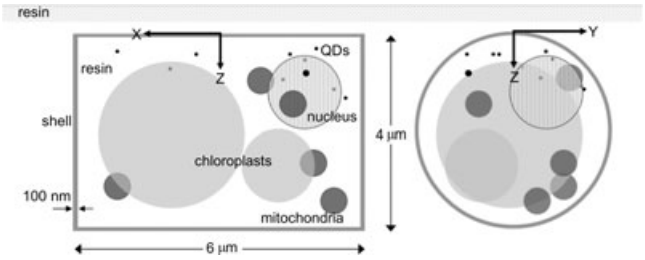

Fig. 1. Monte Carlo simulation model of a diatom with simplified sample geometry: top-down (left) and head-on (right) cross sections. Diatom is embedded in resin some distance below the sample surface. The model consists of nucleus (grey with vertical stripes), mitochondria (dark grey), chloroplasts (light grey), resin (white), quantum dots (QDs; black) and silica shell (outer rectangle and circle in grey). All other organelles are ignored. Material surrounding the diatom is also resin. QDs and the diatom shell are not shown to scale with respect to the other components.

structured silica shell. These diatoms are of interest partly because of their ability to generate micro- and nanoscale silica features (Frigeri *et al.*, 2006). If high-resolution elemental maps can be obtained from the FIB-EDS analysis of diatoms, this information would contribute to the elucidation of the molecular details and the mechanism of the biomineralization process.

NISTMonte provides a framework to define complex sample geometry into a hierarchy of overlapping regions and specify the material properties for each region. This ability to define the sample geometry is well suited for our artefact study because we now have the *a priori* knowledge of the original 3D structure of the model (phantom) that can be used to identify the artefacts in the reconstructed volume and assess their magnitudes. For the simulations in this study, a 100-nm-thick cylindrical shell is used to model the diatom shell. The diatom's internal geometry is simplified by only including the nucleus, the chloroplasts and the mitochondria and assuming a spherical geometry for each organelle. We assume that the diatom is stained with OsO_4 and embedded in resin in order to simulate the common biological electron microscopy sample preparation conditions. Also the intracellular space not bound by organellar membrane is assumed to be resin filled. Figure 1 illustrates the simplified diatom geometry used in the Monte Carlo simulations. In some of the simulations, several single and aggregate CdSe quantum dots (QDs) are included in the model to assess the detection sensitivity of the X-ray analysis technique. Material composition for each cellular component is determined based on the published elemental analysis data of various plant and mammalian cells (Table 1) (Bowen, 1979; Quail, 1979; Sterner & Elser, 2002). Although different organelles are given different elemental compositions, the organelle membrane and the organelle internal composition are not differentiated in the model. Two percent osmium content is assumed for all organelles to account for OsO_4 staining but not included in the silica shell and the resin compositions.

Table 1. Elemental compositions of the model diatom organelles. Organelle membrane composition is combined with the organelle's internal composition.

Material	Composition (weight%)	Density (g/mL)
Resin	C:70, O:28, Cl:2	1.14
Shell	Si:47, O:53	2.2
Mitochondria	C:49.7, O:25.9, N:11, H:7.7, S:0.6, P:3.1, Os:2	1.18
Nucleus	C:41.4, O:28.5, N:16.8, H:7.1, S:0.6, P:3.6, Os:2	1.32
Chloroplast	C:48, O:25, N:12, H:11, S:0.3, P:0.3, Os:2, Mn:0.1, Mg:0.3	1.24

The sequential removal of sample slices by FIB milling is simulated by using multiple diatom models. Each model simulates the position and the condition of the diatom sample after an FIB cut has been made. The first diatom model consists of a resin block where an intact diatom was placed 0.5 μm below the sample surface. In the subsequent models, the removal of the sample material by FIB milling is simulated by placing the diatom closer to the sample block surface and exposing different cross-sectional views of the diatom's internal geometry. Figure 2B shows several of these models, each illustrating a different sample state: diatom fully embedded in the resin block, top of the diatom barely exposed at the surface, a portion of the diatom shell removed and diatom with cellular organelles exposed.

Our Monte Carlo simulations assume a normal incident electron beam and a 40° EDS detector takeoff angle. However, in an experimental setup of FIB-EDS analysis, the sample is usually tilted so that its surface is normal to the ion beam and the electron imaging and the X-ray mapping of the milled surface (which is parallel to the ion beam; not to be confused with the sample surface) are performed at oblique angles. The schematic of a typical FIB-EDS experimental geometry is shown in Fig. 2(A). Also, in laboratory experiments, milling artefacts such as surface damage due to the high energy Ga^+ implantation and the vertical striping of the milled surface (curtaining) can significantly affect and complicate the measurement and the interpretation of the X-ray data (Giannuzzi & Stevie, 2005; Giannuzzi *et al.*, 2005). In our simulations, however, each milled surface is assumed to be perfectly smooth and Ga^+ free.

NISTMonte runs

All simulations were run on two dual processor 3.72 GHz Xeon workstations with 3 GB of RAM running Windows XP[1].

[1] Certain commercial equipment, instruments or materials are identified in this paper to foster understanding. Such identification does not imply recommendation or endorsement by the National Institute of Standards and Technology, nor does it imply that the materials or equipment identified are necessarily the best available for the purpose.

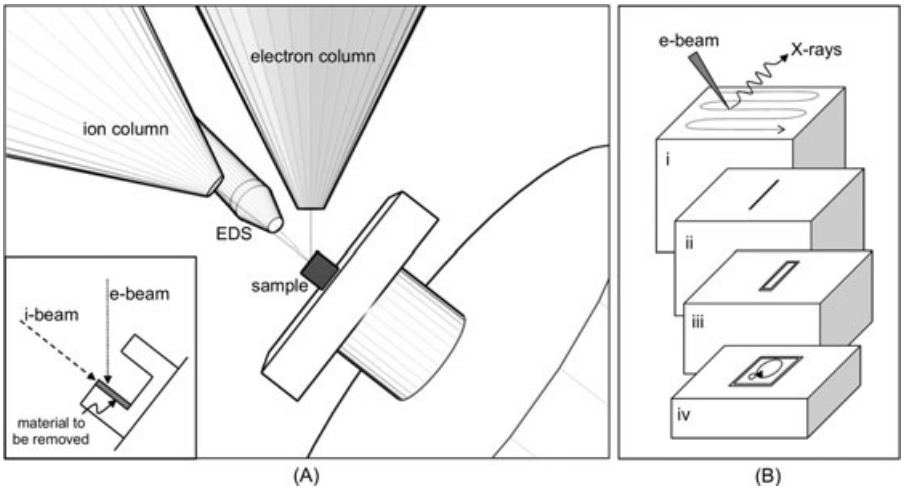

Fig. 2. Schematics of (A) a typical experimental geometry for FIB sectioning and X-ray mapping and (B) the sample models (phantoms) used in the Monte Carlo simulations. In (B), each model represents a resin block containing a resin-embedded diatom where a different amount of the sample material has been FIB milled away: (i) a diatom fully embedded in the resin block, (ii) top of the diatom barely exposed at the surface, a portion of the diatom shell removed, and (iii) + (iv) diatoms with cellular organelles exposed.

Simulation time ranged from several hours to several days depending on the number of energy channels used and the complexity of the sample geometry near the exposed surface. Five sets of simulations were carried out in all. Four of the sets were run at four different beam energies (5, 10, 20 and 30 keV) using the diatom models without QDs and the last set was run at 5 keV with the QD containing diatom models. Beam diameter of 30 nm was used for all simulations.

NISTMonte allows the user to specify the EDS detector type as well as various settings for the detector. All simulations were performed using a Si(Li) detector with 130 eV resolution (full width half max at Mn Kα) 10 eV channel width, 40×10^{-5} sr solid angle and 40° takeoff angle. For other detector characteristics such as window type, thickness of the dead layer, etc., default parameters are used.

Depending on the beam energy, sequential milling of a 100-, 250- or 500-nm-thick layer of material was simulated until the entire diatom sample volume was removed (total of 4.5-μm-thick layer). Higher removal rates were used for the higher beam energy simulations because additional X-ray mapping did not provide added information at these (10, 20 and 30 keV) beam energies. In each set, multiple simulations, corresponding to multiple FIB milled cross-sectional surfaces, were run. Each simulation generated a 64×64 pixel spectrum image of a 10×10 μm surface region centred about the diatom by scanning the electron beam over the entire region of interest in a raster pattern and collecting the X-rays generated from each pixel location. For each pixel in each image, 1000 electron trajectories were simulated.

The last set of simulations was performed using a 5 keV beam and several QDs were included in the diatom models. The QD clusters ranged from 10 to 200 nm in diameter. Since the QDs were localized in the upper region of the diatom, the milling of the bottom half of the diatom was not simulated. Instead, the results from the earlier non-QD 5 keV simulations were used to supplement the missing data in this region. A 100 nm, instead of 250 nm, thick layer was removed at each milling step in these simulations but all other parameters were kept the same as the earlier 5 keV simulations.

Data processing

Each NISTMonte simulation generates a binary data file containing the X-ray spectrum image, a data cube where each pixel of the image consists of an entire X-ray spectrum, from a single sample slice. Preliminary spectrum image analysis was performed on a partial data set to identify energy channels for each elemental map using Lispix (Bright, 2007). Custom MATLAB scripts were used to perform data reformatting, background subtraction and elemental map extraction from the spectrum image data sets and generation of 2D image stacks from extracted maps (MATLAB, 2008). Cd, Cl, Mg, Mn, Os, P, S and Si X-ray map stacks were generated from each set of simulations. Basic image processing such as cropping, contrast enhancement and noise reduction was done in IMAGEJ (Abramoff *et al.* (2004)). A commercial 3D visualization software package AMIRA was used to generate 3D elemental volumes from the X-ray map stacks (AMIRA, 2008). Manual segmentation and slice interpolation were applied to each map stack prior to the 3D volume generation. For the final 3D volume, only the Si, Mg, S and Cd maps were used. Mg maps were used to identify and reconstruct the chloroplasts, Si for the diatom shell, S for all internal organelles and Cd for the QDs. Each elemental volume was overlaid on top of each other to generate the composite 3D elemental volume.

Results and discussion

In this work, we examined the use of FIB-EDS technique for the 3D elemental analysis of biological specimens. We examined the effects of the incident electron beam energy on the quality of the resulting 3D reconstruction of the elemental distribution patterns in a biological specimen. X-ray spectrum imaging of a diatom was simulated at multiple cross-sectional surfaces and at several different beam energies. The resulting elemental maps and the 3D volumes were analysed for artefacts by comparing them against the original diatom model structure.

Elemental maps of all constituent elements exhibit the broadening of cellular features or the loss of spatial resolution due to the sub-surface beam–sample interaction as the beam energy is increased. This trend is clearly illustrated in the side-by-side comparison of Si, S and Mg maps generated with 5, 10 and 20 keV beam energies, shown in Fig. 3. Figure 3(A) is the top view schematic of the sample where the top of an intact diatom is just exposed to the surface ($z = 0$ μm). Figure 3(B) shows the Si, Mg and S maps generated using this sample configuration at three different beam energies. Figure 3(C) is the top view schematic of the sample where the top half of the diatom was milled away ($z = 2$ μm) partially exposing the two chloroplasts. Figure 3(D) shows the corresponding X-ray maps. Si maps of the intact diatom should show a thin vertical line of Si signal if the detected X-ray signals were coming from the surface of the sample only. However, we see a broad stripe of high Si X-ray intensity, indicating that the detected X-ray signals contain the contributions from a larger sub-surface volume. Similar distortions were seen in the Mg and S maps. At $z = 0$ μm, the 5 keV Mg map does not show anything but the 10 keV Mg map clearly shows the larger of the two Mg rich chloroplasts. In the 20 keV Mg map, both chloroplasts are clearly visible although the smaller chloroplast is located

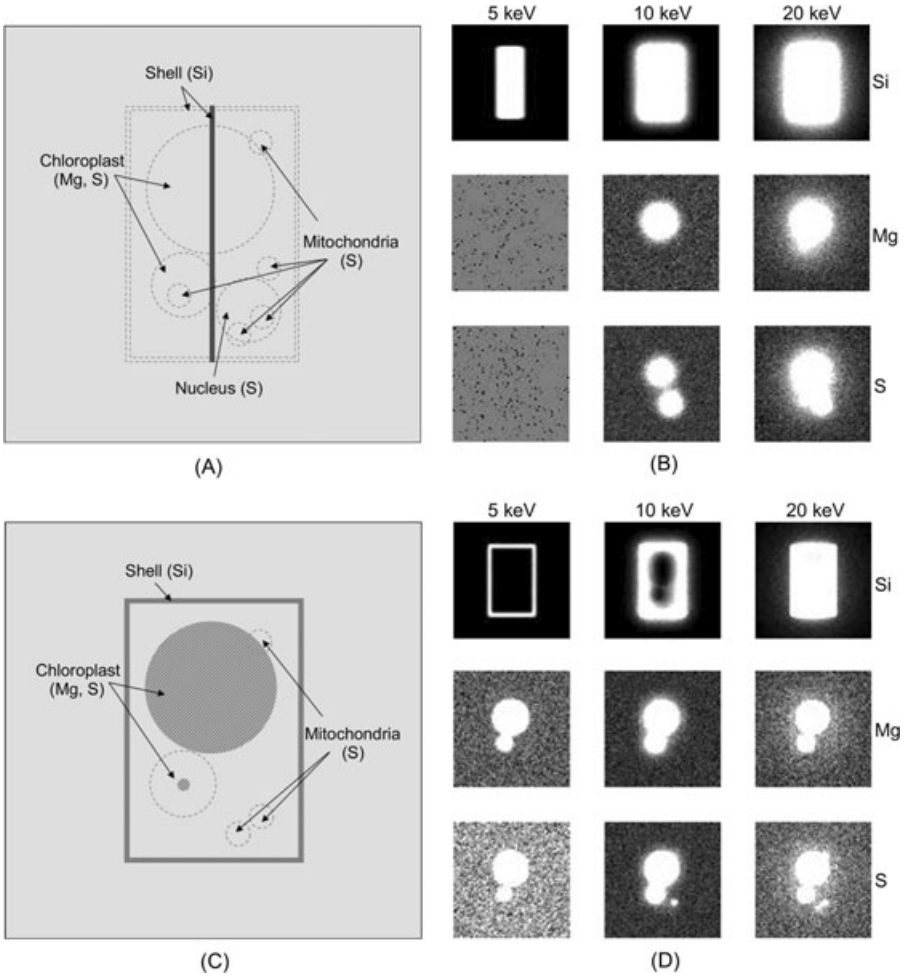

Fig. 3. Elemental maps of a diatom generated from two different cross-sectional locations. (A) is the schematic of the sample geometry at $z = 0$ μm and (B) contains the corresponding Si, Mg and S maps from 5, 10 and 20 keV beam energy simulations. (A) represents the entire X-ray mapping region and the vertical grey line represents the exposed area of the diatom shell. Dashed lines represent the organelles buried under the surface. (C) is the schematic of the sample geometry at $z = 2$ μm (midway through the diatom) and (D) contains the corresponding maps. In (C) and (D), the nucleus and some of the mitochondria have been removed by milling and only the two chloroplasts (grey) and the shell (dark grey) are exposed.

almost 2 μm below the surface. Similarly, 5 keV S map at $z = 0$ μm does not show any features whereas the 10 keV S map shows two circular bodies (chloroplast and nucleus) and the 20 keV S map shows several circular regions all blurred together indicating that the organelles located 2 μm or more below the surface are being detected.

In a true surface analysis technique, only the features that are currently exposed should be visible. However, in the FIB-EDS technique, X-ray signals are generated below the sample surface as the incident electrons penetrate and interact with the sample volume. The sizes of the electron penetration volume and the X-ray generation volume depend on many factors. In general, detected X-rays originate from a volume smaller than the actual X-ray generation volume which is smaller than the electron penetration volume (Goldstein *et al.*, 2003). The detected X-rays reflect the features contained in this detected X-ray volume. Therefore, by looking at the *z*-location (depth) at which each organelle was first detected in the elemental maps, we can estimate the depth range of the detected X-rays or the depth resolution of the FIB-EDS technique for the conditions specified here.

Factors such as the organelle location, concentration of the element in the organelle and the atomic number of the element being detected all contribute to when, or how many μm before the actual features are exposed to the surface, various cellular features become detectable in an X-ray map. The differences between the 'first detection' depth of various organelles and their actual locations can be used to estimate the depth resolution of the FIB-EDS method for the biological applications at different beam energies. Figure 4 shows the plot of the average differences in the detection depth and the actual depth of the organelle. As expected, the depth resolution decreases with the increasing beam energy. At 5 keV, features about 250 nm under the surface are visible but at 30 keV, features several μm below the surface can be detected.

These estimates are also confirmed in the simulated electron trajectories shown in Fig. 5. In these simulations, the top of the diatom is placed at the surface. The incident electron beam is indicated by the vertical down arrows and the electron trajectories in the diatom are depicted as dark lines. In the 5 keV case (Fig. 5A), electrons travel only about 250 nm into the sample before losing most of their energy (50 eV is used as the cutoff threshold). In the 10 keV case (Fig. 5B), electrons reach roughly half way into the diatom and in the higher keV cases (Fig. 5C and D), they can travel through the diatom and exit from the far side of the diatom. In all cases, some X-rays are generated close enough to the sample surface to escape the sample volume. In the 5 keV case, most of the X-rays generated are near the point of beam incidence. However, as the beam energy increases, more X-rays are generated at locations far from the beam incidence point, thus contributing to the loss of spatial resolution.

The 3D volumes generated from the Si, Mg and S X-ray map stacks are shown in Fig. 6. The effects of increasing beam–

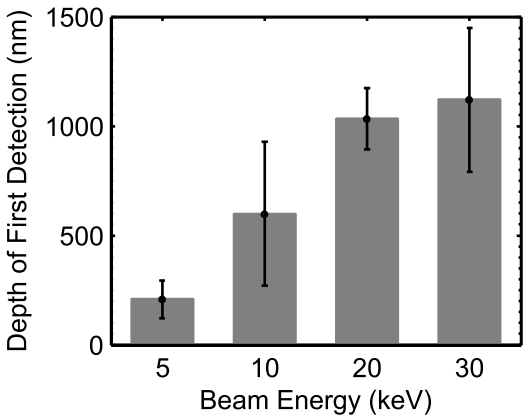

Fig. 4. Effects of beam energy on the average depth of first detection. The first detection depth is the maximum depth at which a feature can be located and still be detected in the X-ray maps. The results are mean values ± SD ($n = 18$).

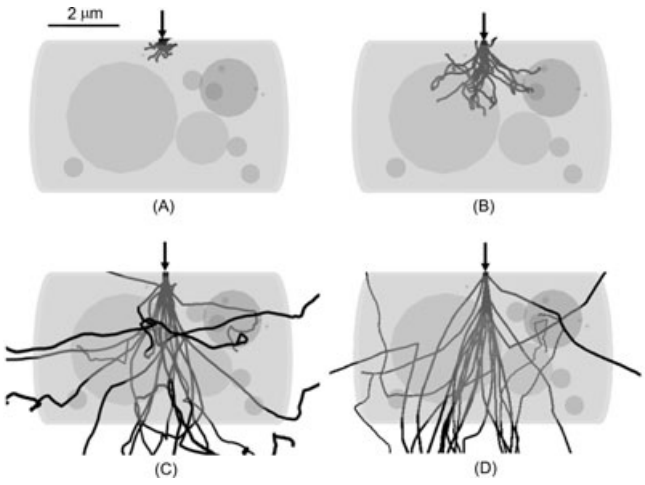

Fig. 5. Simulated electron trajectories at (A) 5 keV, (B) 10 keV, (C) 20 keV and (D) 30 keV beam energies. Black arrow on top of the diatom represents the incident electron beam and the dark lines in and around the diatom are the simulated electron trajectories with a 50 eV cutoff threshold.

sample interaction volume are pronounced here. Fig. 6(A) is the schematic of the original model of the diatom. The 3D volume reconstructed from the 5 keV X-ray maps (Fig. 6B) show some distortions in the diatom shell and the organelles as well as general broadening of internal features. However, the major cellular components are identifiable and appear distinct from each other. In the 10 keV case (Fig. 6C), the distortions due to the increased beam–sample interaction volume become severe enough that the organelle shapes are completely lost, although regions of high Mg or Si concentration are recognizable. Finally in the 20 keV case (Fig. 6D), all elemental volumes overlap each other and none of the organelles are recognizable.

Simulations using the QD-containing models were performed to assess the suitability of the FIB-EDS technique

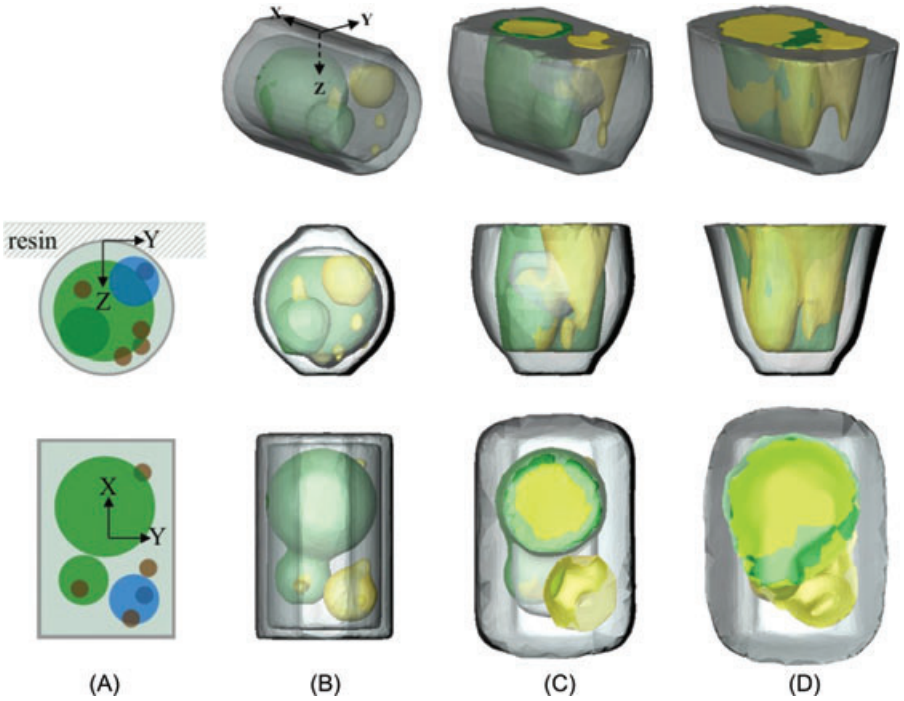

Fig. 6. (A) Head-on and top-down views of the diatom showing the chloroplasts (green), mitochondria (brown), nucleus (blue), shell (grey) and resin (pale green). 3D elemental volumes from the (B) 5 keV, (C) 10 keV and (D) 20 keV beam energy simulations. Mg (green), Si (grey) and S (yellow) volumes are used to generate the composite structures.

for nanoparticle detection in bulk biological specimens. For the QD-containing models, only the 5 keV beam energy simulations were performed since the earlier simulations clearly demonstrated that higher beam energy will not provide sufficiently resolved 3D information. For these simulations, a 100 nm thick slice was removed each time. Figure 7 shows the reconstructed volume based on these X-ray maps. Figure 7(A) represents the original diatom model containing the QDs. The radius of each QD or QD clusters is specified in the figure. Figure 7(B) is the reconstructed volume based on the Si, Mg, S and Cd X-ray maps. The 100 and 200 nm QD clusters are easily detected but the 10 and the 20 nm QDs are not visible in the X-ray maps. Additional simulations shows 50 nm QD clusters are easily detected as well although these clusters are not included in the 3D mapping models shown in Fig. 7.

The two 100 nm QD clusters on the right-hand side of the diatom model in Fig. 7(A) are shown as a single cluster of QDs. In the original QD containing diatom model, these two QD clusters are separated by 150 nm laterally and 130 nm vertically. One cluster is located inside the nucleus and the other is just outside the nucleus. However, as shown in Fig. 7(B), the inherent broadening of the feature due to the beam–sample interaction and the poor mapping pixel resolution (156 × 156 nm per pixel) make them appear as a single larger QD cluster that spans the boundary of the nucleus. A beam–sample interaction volume usually has a

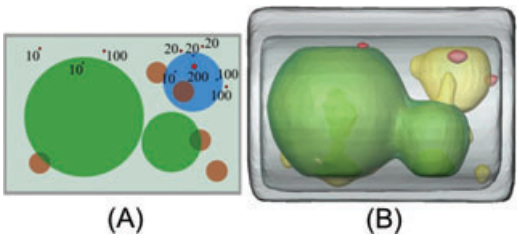

Fig. 7. (A) Side views of the original diatom model showing the chloroplasts (green), mitochondria (brown), nucleus (blue), shell (grey), resin (pale green) and the QDs (red). The diameters (in nm) of the QD clusters are shown in the diagram. (B) Reconstructed volume based on 5 keV Si (grey), Mg (green), S (yellow) and Cd (red) X-ray maps.

larger depth penetration range than the lateral penetration range in low-density materials such as biological samples. The lateral range of the detected X-rays generated by a 5 keV beam is approximately 250 nm in carbon and 50 nm in cadmium (Kanaya & Okayama, 1972; Goldstein *et al.*, 2003). Therefore the lateral X-ray range is expected to fall between 250 and 50 nm in the diatom sample. The lateral resolution of the maps may be improved somewhat by increasing the mapping pixel resolution. However, when increasing the pixel resolution in an actual experimental situation, factors such as the increased mapping time and the loss of resolution due to a sample drift should also be considered.

Several additional factors should be considered when designing an FIB-EDS experiment for the laboratory. X-ray microanalysis of biological samples is plagued by low count rates. When limited to a specific beam energy, the typical solution to this problem is to use a higher beam current or to increase the mapping time. Because biological samples are beam sensitive, increasing the beam current can quickly damage the sample. And, as mentioned earlier, increasing the mapping time can result in the loss of resolution due to a sample drift. Another important factor to consider is the limitations dictated by the instrument geometry. The analysis presented in this study assumes that the electron beam is normally incident on the milled sample surface and the EDS detector is placed at 40° takeoff angle. However, in laboratory FIB-EDS experiments, the electron beam usually is not normally incident and the EDS detector takeoff angle might not be optimal unless additional stage movements are executed (Shaffer *et al.*, 2007). The changes in the beam incident angle and the EDS detector takeoff angle can significantly affect the quality and the resolution of an X-ray map.

Performing X-ray microanalysis at 5 keV is not without challenges. The usual rule of thumb is that to adequately excite an X-ray resulting from a vacancy in a shell with edge energy E_E, the incident beam energy must be greater than or approximately equal to 1.5 times E_E. This suggests that at 5 keV we can efficiently excite X-rays with energies below about 3 keV. The lowest energy X-ray which is commonly measured using an EDS detector is the B Kα at around 200 eV. The Kα lines for elements between B ($Z = 5$) and Ar ($Z = 18$), the Lα lines between Sc ($Z = 21$) and Ag ($Z = 47$) and an M line between Ce ($Z = 58$) and Ac ($Z = 89$) are visible in EDS spectra and fall between 200 eV and 3 keV. Although these lines do cover most of the periodic table, it represents a large number of lines in such a small energy range which can make unambiguous identification challenging. Furthermore, lower energy lines tend to be strongly absorbed by matter between the point of generation and the detector, further complicating accurate quantification.

Conclusions

Although the beam–sample interaction is a well known problem in the X-ray microanalysis field, its effects have not been analysed carefully for the purpose of 3D volumetric analysis of biological specimens. In this work, we studied the effects of different beam energies for generating 3D X-ray maps of biologically relevant specimens and evaluated the detection and resolution limitations of the FIB-EDS technique for this type of sample. Based on our analysis, for the 3D elemental analysis of resin-embedded bulk biological samples and the conditions specified in this study, 5 keV beam energy is likely to be the maximum usable X-ray mapping beam energy. Even at 5 keV, 3D reconstruction suffers from noticeable distortions in the features due to the sub-surface beam–sample interactions. However, the general shape and the size of the features are reproduced reasonably well at 5 keV beam energy. Maps generated using beam energies higher than 5 keV produce unrecognizable 3D cellular features.

Detection of nanoparticles in biological systems using X-ray microanalysis was also considered. 100 nm or larger diameter particles were easily detected but a single nanoparticle or a small cluster of nanoparticles was not detected using the FIB-EDS technique. Also the nanoparticles that were close together were incorrectly identified as a single larger cluster of nanoparticles. For example, nanoparticles that are on either side of an organelle membrane, which is about 10 nm thick, might be difficult to resolve using this technique. Overall lateral and depth resolutions of the X-ray mapping of biological specimen are on the order of 100 and 250 nm, respectively, when using a 5 keV beam. Finer milling steps and higher lateral sampling frequency can provide limited improvements in the spatial resolution but at the expense of a longer mapping time. Also the high-resolution SEM images corresponding to the X-ray maps can be leveraged to yield composite images with an improved effective X-ray resolution.

By improving the milling resolution and by supplementing the lower resolution X-ray maps with the corresponding high-resolution structural data from SEM images, FIB-EDS can provide more detailed elemental and structural information than existing methods. However, the proper acquisition and the interpretation of X-ray mapping data depend on many factors such as the beam parameters, detector settings, sample composition, fixing and staining methods and embedding material. Models used in this work are relatively simple representations of a diatom. In addition, our simulations are based on a single organism and we cannot generalize our results to all possible biological specimens. Work is still needed in generating accurate and diverse biological models as well as simulating experimental conditions relevant to these samples. However, based on these simulations, we have been able to establish baseline X-ray mapping conditions that can provide reasonable results for bulk biological samples such as diatoms.

References

Abramoff, M.D., Magelhaes, P.J. & Ram, S.J. (2004) Image processing with Image. *J. Biophotonics International* **11**, 36–42.

Alirol, E. & Martinou, J.C. (2006) Mitochondria and cancer: is there a morphological connection? *Oncogene* **25**, 4706–4716.

Amira (2008) http://www.amiravis.com/index.html. Visage Imaging, Carlsbad, CA. Last accessed: 07/01/2009.

Baumeister, W. (2002) Electron tomography: towards visualizing the molecular organization of the cytoplasm. *Curr. Opin. Struct. Biol.* **12**, 679–684.

Bowen, H.J.M. (1979) *Environmental Chemistry of the Elements*, pp. 106–107. Academic Press. London.

Bright, D. (2007) *Lispix*. http://www.nist.gov/lispix/doc/contents.htm. Last accessed: 07/01/2009.

Echlin, P. (1992) *Low Temperature Microscopy and Analysis*, pp. 424–430. Plenum Press. New York.

Frank, J. (1992) *Electron Tomography*. Plenum Press. New York.

Frigeri, L.G., Radabaugh, T.R., Haynes, P.A. & Hildebrand, M. (2006) Identification of proteins from a cell wall fraction of the diatom Thalassiosira pseudonana: insights into silica structure formation. *Mol. Cell. Proteomics* **5**, 182–193.

Gauvin, R., Lifshin, E., Demers, H., Horny, P. & Campbell, H. (2006) Win x-ray: a new Monte Carlo program that computes x-ray spectra obtained with a scanning electron microscope. *Microsc. Microanal.* **12**, 49–64.

Giannuzzi, L.A. & Stevie, F.A. (2005) *Introduction to Focused Ion Beams*, pp. 13–52. Springer. New York.

Giannuzzi, L.A., Geurts, R. & Ringnalda, J. (2005) 2 keV Ga+ FIB milling for reducing amorphous damage in silicon. *Microsc. Microanal.* **11**(Suppl 2), 828–829.

Giannuzzi, L.A., Phifer, D., Giannuzzi, N.J. & Capuano, M.J. (2007) Two-dimensional and 3-dimensional analysis of bone/dental implant interfaces with the use of focused ion beam and electron microscopy. *J. Oral. Maxillofac. Surg.* **65**, 737–747.

Goldstein, J., Newbury, D., Joy, D. *et al.* (2003) *Scanning Electron Microscopy and X-Ray Microanalysis*, pp. 61–98, 271–296. Plenum Press. New York.

Gustafsson, M.G.L. (2005) Nonlinear structured-illumination microscopy: wide-field fluorescence imaging with theoretically unlimited resolution. *Proc. Natl. Acad. Sci.* U.S.A. **102**, 13081–13086.

Hell, S.W. (2003) Toward fluorescence nanoscopy. *Nat. Biotech.* **21**, 1347–1355.

Heymann, J.A.W., Hayles, M., Gestmann, I., Giannuzzi, L.A., Lich, B. & Subramaniam, S. (2006) Site-specific 3D imaging of cells and tissues with a dual beam microscope. *J. Struct. Biol.* **155**, 63–73.

Holzer, L., Indutnyi, F., Gasse, P.H., Munch, B. & Wegmann, M. (2004) Three-dimensional analysis of porous $BaTiO_3$ ceramics using FIB nanotomography. *J. Microsc.* **216**, 84–95.

Hovington, P., Drouin, D. & Gauvin, R. (1997) CASINO: a new Monte Carlo code in C language for electron beam interaction – part I: description of the program. *Scanning* **19**, 1–14.

Jiang, W., Baker, M.L., Jakana, J., Weigele, P.R., King, J. & Chiu, W. (2008) Backbone structure of the infectious e15 virus capsid revealed by electron cryomicroscopy. *Nature* **451**, 1130–1135.

Joy, D.C. (1995) *Monte Carlo Modeling for Electron Microscopy and Microanalysis*. Oxford University Press. New York.

Kanaya, K. & Okayama, S. (1972) Penetration and energy-loss theory of electrons in solid targets. *J. Phys. D: Appl. Phys.* **5**, 43–58.

Kotula, P.G., Keenan, M.R. & Michael, J.R. (2006) Tomographic spectral imaging with multivariate statistical analysis: comprehensive 3D microanalysis. *Microsc. Microanal.* **12**, 36–48.

Leapman, R.D., Kocsis, E., Zhang, G., Talbot, T.L. & Laquerriere, P. (2004) Three-dimensional distributions of elements in biological samples by energy-filtered electron tomography. *Ultramicroscopy* **100**, 115–125.

Lefurgey, A., Bond, M. & Ingram, P. (1988) Frontiers in electron probe microanalysis: application to cell physiology. *Ultramicroscopy* **24**, 185–220.

Marsh, B.J., Mastronarde, D.N., Buttle, K.F., Howell, K.E. & McIntosh, J.R. (2001) Organellar relationships in the Golgi region of the pancreatic beta cell line, HIT-T15, visualized by high resolution electron tomography. *Proc. Natl. Acad. Sci.* U.S.A. **98**, 2399–2406.

MatLab. (2008) http://www.mathworks.com/products/matlab. The MathWorks, Natick, MA, USA. Last accessed: 07/01/2009.

McEwen, B. & Marko, M. (2001) The emergence of electron tomography as an important tool for investigating cellular ultrastructure. *J. Histochem. Cytochem.* **49**, 553–563.

McIntosh, R., Nicastro, D. & Mastronarde, D. (2005) New views of cells in 3D: an introduction to electron tomography. *Trends Cell Biol.* **15**, 43–51.

Myklebust, R., Newbury, D. & Yakowitz, H. (1976) NBS Monte Carlo electron trajectory calculation program. *NBS Special Publication 460* (ed. by K. Heinrich, H. Yakowitz. & D. Newbury), pp. 105–125. National Bureau of Standards, Washington DC.

Quail, P.H. (1979) Plant cell fractionation. *Ann. Rev. Plant Phys.* **30**, 425–484.

Ritchie, N.W.M. (2005a) A new Monte Carlo application for complex sample geometries. *Surf. Interface Anal.* **37**, 1006–1011.

Ritchie, N.W.M (2005b) Spectrum simulation with NISTMonte. *Microsc. Microanal.* **11**(Supp 2), 1290–1291.

Ritchie, N.W.M. (2008) *NISTMonte*, http://www.cstl.nist.gov/div837/837.02/epq/index.html. Last accessed: 07/01/2009.

Rust, M.J., Bates, M. & Zhuang, X. (2006) Sub-diffraction-limit imaging by stochastic optical reconstruction microscopy (STORM). *Nat. Meth.* **3**, 793–795.

Salvat, F., Fernández-Varea, J.M. & Sempau, J. (2006) *PENELOPE – A Code System for Monte Carlo Simulation of Electron and Photon Transport*. OECD Nuclear Energy Agency, Issy-les-Moulineaux.

Shaffer, M., Wagner, J., Schaffer, B., Schmied, M. & Mulders, H. (2007) Automated three-dimensional x-ray analysis using a dual-beam FIB. *Ultramicroscopy* **107**, 587–597.

Shroff, H., Galbraith, C.G., Galbraith, J. *et al.* (2007) Dual-color superresolution imaging of genetically expressed probes within individual adhesion complexes. *Proc. Natl. Acad. Sci.* U.S.A. **104**, 20308–20313.

Sterner, R.W. & Elser, J.J. (2002) *Ecological Stoichiometry*, pp. 71–72. Princeton University Press. Princeton.

Subramaniam, S. (2005) Bridging the imaging gap: visualizing subcellular architecture with electron tomography. *Curr. Opin. Microbiol.* **8**, 316–322.

Svergun, D.I. & Koch, M.H.J. (2002) Advances in structure analysis using small-angle scattering in solution. *Curr. Opin. Struct. Biol.* **12**, 654–660.

Uchic, M., Holzer, L., Inkson, B.J., Principe, E.L. & Munroe, P. (2007) Three-dimensional microstructural characterization using focused ion beam tomography. *MRS Bull.* **32**, 408–416.

Volkert, C.A. & Minor, A.M. (2007) Focused ion beam microscopy and micromachining. *MRS Bull.* **32**, 389–395.

Zierold, K., Michel, J., Terryn, C. & Balossier, G. (2005) The distribution of light elements in biological cells measured by electron probe x-ray microanalysis of cryosections. *Microsc. Microanal.* **11**, 138–145.

